Estimation of the Temperature in the Stirred Zone and Cooling Rate of Friction Stir Welding of EH46 Steel from TiN Precipitates

Al-moussawi, M., Smith, A., Faraji, M. & Cater, S.

Original citation & hyperlink:
Al-moussawi, M, Smith, A, Faraji, M & Cater, S 2019, 'Estimation of the Temperature in the Stirred Zone and Cooling Rate of Friction Stir Welding of EH46 Steel from TiN Precipitates', Metallurgical and Materials Transactions A, vol. 50, no. 11, pp. 5103-5116.

DOI 10.1007/s11661-019-05383-x
ISSN 1073-5623
ESSN 1543-1940

Publisher: Springer

The final publication is available at Springer via http://dx.doi.org/10.1007/s11661-019-05383-x

Estimation of the Temperature in the Stirred Zone and Cooling Rate of Friction Stir Welding of EH46 Steel from TiN Precipitates

Montadhar Al-moussawi, ** Alan J. Smith, ***[1] Masoumeh Faraji, * Stephen Cater,**

Al-Furat Al-Awsat university, Iraq; **Sheffield Hallam University, Sheffield, S1 1WB, UK; ***Coventry University, Coventry, CV1 2JH, UK; ** TWI Yorkshire Technology Centre, Rotherham, S60 5TZ, UK**
Corresponding email: [1]masoumeh.faraji@coventry.ac.uk

Abstract

Measuring the peak temperature in the contact region of the tool/workpiece in friction stir welding (FSW) is difficult using conventional methods such as use of thermocouples or a thermal imaging camera, hence an alternative method is required to tackle this problem. The objective of the present work was to estimate more accurately, for the first time, the peak temperature and cooling rate of FSW from precipitation of TiN in friction stir welded steel samples. Microstructures of nine friction stir welded samples of high strength shipbuilding steel of EH46 grade were examined closely by SEM-EDS to detect the TiN precipitates. Thermal heat treatments using an accurate electrical digital furnace were also carried out on 80 unwelded EH46 steel samples over a range of temperatures and cooling rates. Heat treatments were to create a basis to understand TiN precipitation behavior under various heating and cooling regimes for the studied alloy. Heat treatment showed that TiN particles can precipitate at a peak temperature exceeding 1000°C and the size of TiN precipitates particles increases with decreasing cooling rate. In a temperature range between 1100-1200°C the TiN precipitates were accompanied by other elements such as Nb, S, Al and V. Pure TiN particles were found after the peak temperature exceeded 1250°C with limited precipitation after reaching a peak temperature of 1450°C. The comparison between the friction stir welding samples and the heat treatments in terms of types and sizes of TiN precipitates suggests that the welding peak temperature should have been in the range of 1200-1350°C with a cooling rate in the range of 20-30 K/sec. The current work represents a step change in estimating the friction stir welding temperature and cooling rate which are difficult to determine using thermocouples and thermal imaging camera.

Keywords: Friction Stir Welding (FSW), EH46 steel, TiN precipitates, Peak temperature, Cooling rate.

1-Introduction

Friction stir welding (FSW) which was invented in the UK/TWI in 1991 [1] is still a challenge when utilized for high melting alloys such as steel. In addition to the high cost of the tools, the prime challenge is to select suitable welding parameters to produce sound welds. The most important factor in the FSW process is to find the right temperature required to make the steel yield under specific tool rotational and traverse speeds during welding. Determination of this temperature in the workpiece/tool contact region during friction stir welding is usually difficult. Thermocouples (TC_s) which are usually used for this purpose cannot be placed directly in the stir zone region because they will be damaged or displaced by the deforming material in the stir zone before recording the peak temperature, leading to inaccurate measurements. Moreover, thermocouples attached to the top surface adjacent to the edge of the stir zone are often severed by extrusion of the flash from under the tool shoulder before reaching peak temperature. An earlier study has used thermocouples to measure the temperature of the contact region for friction stir welding of an aluminum alloy (AA6061-T6) [2]. They have, however, drilled eight holes with 1.5 mm diameters at different positions of the work-piece to insert TCs. Using a thermal imaging camera for measuring the temperature of work-piece during FSW is also difficult and cannot produce accurate data. This is because the field of view of the camera can

be restricted by the presence of the argon gas shield applied to the weld area, and the presence of clamps that is holding down the workpiece. The camera also has no direct view of the tool itself, and measuring the temperatures on the surface of the plate adjacent to the weld area, using camera, gives data that are unrepresentative of the internal weld temperatures. Finally, the emissivity of the tool can change significantly during the weld process and thus accurate calibration of the camera is also another significant drawback.

Elsewhere Carlone and Palazzo [3] have used an infrared thermal camera, fixed on the machine and focused on the leading edge, to determine the surface temperature of the weld in an AA2024-T3 alloy. However, they have not discussed the reproducibility and level of precision of their measurements. For the rotational (ω) and traverse (υ) speeds of 800 rpm and 140 mm/min they have reported a peak temperature of 475°C. More recently Mezyk and Kowieski [4] have used short wave infrared camera mounted on the FSW mill to detect discontinuities in the FSW workpieces and also to monitor the temperature. They have reported appearance of excessive "burr" on both sides of the weld where part of the burr (a shaving) was pushed out behind the tool which caused disturbances on thermograms (camera's recorded data); such disturbances caused a jump of 100°C in the temperature profile along the measurement line. Hence, they described this technique as a qualitative method which still needs further development.

Compared to direct temperature measurements, using an analytical approach, Zhang et al [5] have used the equation developed by Arora et al [6], presented below, to calculate the peak temperature (T, °C) in FSW of AA2024-T3 alloys.

$$T = (0.151 \log_{10}\left(\frac{\sigma_8 A \omega C \eta}{\lambda \upsilon^2}\right) + 0.097)\,(T_s - T_r) + T_r \quad (1)$$

where T_s is the solidus temperature, T_r is the initial temperature, ω and ν are rotational and traverse speeds, σ_8 is the yield stress of the material at a temperature of $0.8T_s$, A is the cross-sectional area of the tool shoulder, C and λ are the specific heat capacity and thermal conductivity of the workpiece material, respectively, and η is the ratio of generated heat at the shoulder/workpiece interface, transported between the tool and the workpiece.

They have estimated the peak temperature under welding speeds of ω and υ of 800 rpm and 140 mm/min to be 455°C. Moreover, Wang et al [7] measured the peak temperature of FSW plates of AA2024-T4 using thermocouples. They have reported peak temperature of 425°C for ω and υ of 750 rpm and 150 mm/min. These conditions are very similar to the above-mentioned study where thermal camera has been used to measure the peak temperature, however, the reported peak temperature measured using thermal camera is significantly higher. Therefore, the reliability of thermal camera for FSW temperature measurements should be questioned.

In the present work, the use of a new off-line method which depends on the formation of TiN precipitates during the heating-cooling cycle of FSW is investigated. Clearly, the existence of TiN particles is dependent on the process of as-received materials. TiN particles are diminished at faster cooling rates during solidification [8]. This method is to enable a more accurate estimation of the peak temperature at the interface as well as cooling rate of the sample after the welding is completed. It is also an accurate and inexpensive alternative method compared with the use of thermocouples and thermal imaging camera.

In order to use the suggested off-line method, it is of paramount importance to understand how and when TiN particles precipitate and appear in steel grades, particularly in low alloy grades similar to the grade used in this work. Precipitation of TiN during heating and cooling cycles in various steel grades have been studied previously mostly during solidification, pre-deformation heating and post deformation. Stock et al. [8] investigated the cooling rate effects on TiN precipitates in low carbon steel during and after solidification and found that TiN particles can precipitate at very high temperatures near the melting point of the steel. They also found that TiN particles size increases with decreasing cooling rates and the precipitate size

can reach 1-2.5 μm at low cooling rates (0.1 K/s), whereas, particles tend to cluster for higher cooling rates (600 K/s). Nagata et al. [9] studied the TiN particles distribution in a thin-slab cast HSLA steel grade (similar to the grade studied here) using TEM examination. They found that TiN precipitate size decreased with increasing post solidification cooling rate. Using TEM and electrolytic chemical analysis and focusing on formation temperature of Ti particles El-Fawakhry et al. [10] studied TiN precipitation in microalloyed steels with Ti, subjected to hot rolling. They found TiN precipitates of 5-10μm in samples taken from alloys hot rolled at 1250°C. It is believed that due to high stability of TiN, it precipitates at very high temperatures, most probably in the molten state as coarse precipitates. Wang et al. [11] found that in low carbon steel the TiN particles nucleated on Ti_2O_3 -particles. Hong et al. [12] studied the evolution of precipitates in Nb-V-Ti microalloyed steel in a temperature range of 1100-1400°C using TEM. Their study found that (Ti,Nb)(C,N) carbonitrides disappeared after reheating the alloy in a temperature range higher than 1000°C and a new cubic shape particles precipitated in the microstructure with a size depending on the peak temperature and cooling rate. They found that as reheating temperature increased from 1050 to 1400°C, Nb content within precipitates decreased; however, Ti content did not alter till 1250°C and above 1300°C, Ti began to dissolve into the austenite matrix. All these studies [10-12] suggest that in low carbon low alloy steel, TiN won't dissolve in temperatures below 1200°C. In alloys similar to the grade studied here, this can provide a basis for a minimum temperature above which TiN can be found.

The current study aims to identify TiN precipitates in the microstructure of samples taken from stirred zones of FS welded of high strength shipbuilding EH46 steel plates using SEM-EDS. Such precipitates are to be compared with precipitates formed in heat treated un-welded samples of the same steel grade with the same thickness. Heat treatments are conducted under various thermal and cooling regimes to enable simulation of various peak temperatures and cooling rates of the welded counterparts.

It is worth noting that, although FSW is a thermomechanical process, the strain rate effect has not been taken into consideration in the heat treatment procedures. However, it is expected that strain rate will influence mainly the incubation time of phase transformation and elemental precipitation/segregation. This theory is supported by previous works carried out on steel where in addition to heat treatments strain rates (using methods such as hot compression, rolling and FSW) were applied. They have shown that the phase changes [13] and elemental precipitation occur faster when the process includes strain rate in addition to the heating; e.g. in microalloyed steels at greater strains, the incubation and completion time for precipitation are shorter ([14-15]). Failla et al. [13] studied the effect of deformation on the phase transformation of ferrite and bainite in HSLA-65 alloy during FSW process and found that phase transformation occurs faster when deformation increases. Upon application of deformation austenite grain size was reduced during the FSW process which promoted the formation of ferrite. The incubation time of Nb(C,N) elemental precipitation has also been studied by Zhu and Qiu [15], in a microalloyed steel during continuous cooling, which was found to decrease with an increase in strain rate. The time of precipitation was reduced from 6000 secs to 3548 secs with the casting speed increasing from 0.9m/min to 2.4m/min whereas, the temperature of precipitation onset remained constant [15].

The main aim of this work is to implement a simpler method to determine the peak temperatures of EH46 FS welded samples by studying TiN precipitation in this alloy. It is also to produce a known list of few peak temperatures and cooling rates of such steel grade from TiN precipitates sizes. This procedure can be used to select the best tool rotational and traverse speeds that generate desirable temperatures during FSW and thus to control the process more readily.

2-Materials and Methods

The chemical composition (wt%) of EH46, which is an Nb-V microalloyed low Sulphur steel, as provided by the manufacturer, is shown in Table 1.

2.1 FSW Samples

Nine FS welded samples were produced from plates of EH46 grade (14.8 mm thickness) at TWI Technology Centre in Yorkshire using PowerStir welding machine equipped with Poly Crystalline Boron Nitride (PCBN) hybrid tool. The tool consisted of a shoulder with a diameter of 38mm and probe with a length of 12mm. Out of these samples seven specimens were produced under plunge and dwell welding conditions and the remaining two were welded under steady state condition. Their positioning is shown in Figure 1. The plunge trial welds are denoted as W1 to W7 and the steady state trials are coded as W8 and W9. The welding parameters for the plunge/dwell and steady state conditions are shown in Tables 2 and 3, respectively.

Table 1: Chemical composition (wt%) **of EH46 Steel Grade as received (composition is provided by the manufacturer).**

C	Si	Mn	P	S	Al	N	Nb	V	Ti
0.20	0.55	1.7	0.03	0.03	0.015	0.02	0.03	0.10	0.02

Figure 1: Representation of the positioning of the seven plunge trials for EH46 steel plates.

Table 2: The welding parameters for FS welded EH46 plunge/dwell samples (W1-W7).

Weld Trial No.	Tool rotational speed ω (RPM) at dwell period	Max. Axial (Plunge) force (F_z) KN	Max. longitudinal force (F_x) KN	Max. Torque (M) N.m	Plunge Depth (Z) mm from FSW machine	Dwell Time (t) sec at dwell period
W1	200	157	17	498	13	6
W2	200	127	17	471	13	8
W3	120	116	21	598	13	7
W4	120	126	20	549	13	6
W5	120	115	17	532	13	7
W6	120	105	18	583	13	7
W7	120	119	20	548	13	7

Table 3: Welding parameters for FS welded EH46 steel at steady state condition (W8 and W9).

Tool rotational speed RPM	Traverse speed mm/min	Rotational/ Traverse speeds (rev/mm)	average spindle Torque N.m	average tool Torque N.m	Axial force (average) KN	longitudinal force (average) KN	Representation of Heat Input $(\frac{\omega \times torque}{V})$ (rev. KN)
150	50	3	300	114	66	13	342
150	100	1.5	450	171	72	14	256.5

2.2 Heat Treated Samples

Heat treatments were conducted on 80 samples of EH46 steel, each sample was a cube of 14.8 mm in length. The heat treatments were carried out in a calibrated electric furnace at temperatures ranging from 1000 to 1500°C and at holding times of approximately 10 to 30 sec. Samples were placed in the center of the furnace and the surface temperature of the sample under study was measured by an attached thermocouple connected to a digital 4-channel data logger thermometer. Different cooling rates were applied including quenching in oil (90K/sec), quenching in hot oil with a temperature of 150°C (30K/sec), still air cooling and cooling inside the furnace (0.35K/sec). The values for cooling rates of different media are determined using temperature profile of samples obtained by thermocouples attached to their surface.

2.3 SEM - EDS

Scanning electron microscopy (SEM) examination was carried out on polished and etched (with 2% Nital) friction stir welded and also heat treated samples. SEM produced high quality and high resolution images of micro constituents by employing secondary electron (SE) imaging mode with accelerating voltages of 10 to 20 kV which provides high penetration. The working distance (WD) used was 10 mm but in some cases, it was altered (decreased or increased) to enhance the contrast at higher magnification. Energy Dispersive Spectroscopy EDS (point and ID) based on SEM was used to detect the Ti precipitates. The changes in Prior Austenite Grain Size (PAGS) with temperature have been measured using the linear intercept method (ASTM E-112). To find each average value of PAGS, about 5 to 7 images were taken and measured carefully. The TiN particles diameter and their distribution were measured by applying square grid using image grid software in which the number of intersections of the grid falling in the TiN particles were counted and compared with the total number of points laid down. When measuring average size of TiN particles for each condition 7 images were taken separately in dimensions of 600 μm by 600 μm and then they were used in image grid software.

3-Results

3.1 Prior Austenite Grain Size (PAGS) and Temperature

To understand the role of temperature on the prior austenite grain size (PAGS) Figure 2 illustrates the relationship between peak temperature and PAGS for holding time of 30 sec.

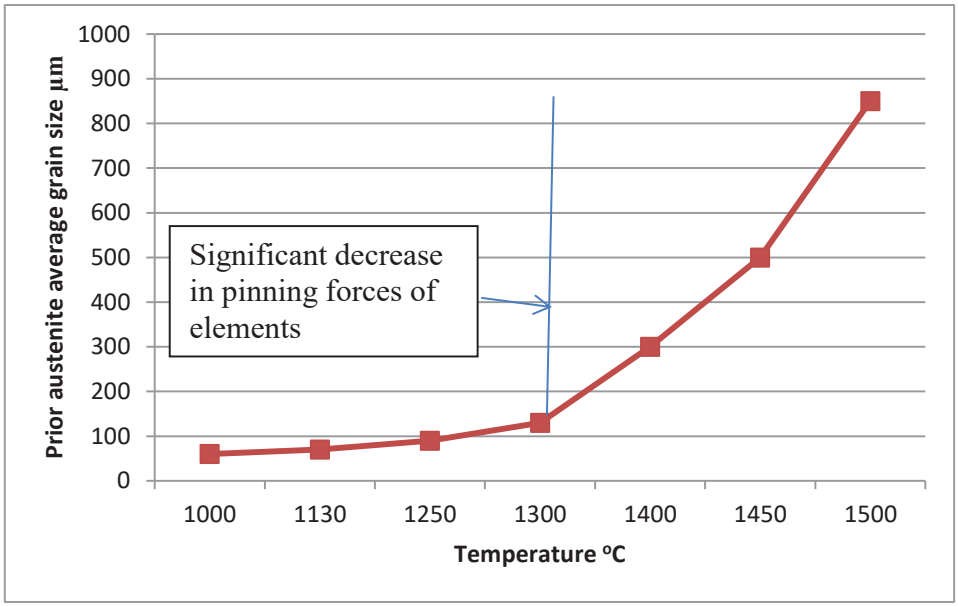

Figure 2: Variation of prior austenite grain size with temperature for heat treated samples of EH46 in temperature range of 1000-1500 °C with holding time of 30sec.

3.2 TiN precipitates in the heat treated samples

Figure 3 is a high magnification SEM image of the as-received EH46 which shows particles containing Ti. However, SEM observations did not show any cube shaped TiN in the as-received samples. Figures 4 to 6 show the presence of Ti precipitates in a given sample heat treated at temperatures of 1130°C, 1250°C and 1400°C respectively. They show that with increasing heat treatment temperature the content of the precipitates changes, with leaving only Ti and N at 1400°C. Figure 7 shows TiN particles are precipitated after heating the sample to 1240°C followed by oil quenching.

Figure 3: SEM micrograph showing Ti and Ti-Nb based particles in the as-received EH46.

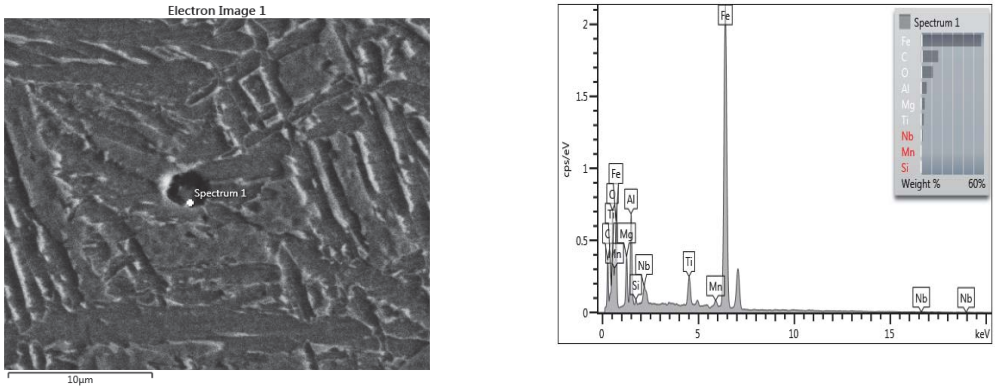

-a- -b-

Figure 4: EH46 sample, heated to 1130 º C for 1min, followed by hot oil quenching (30K/sec)**, a-SEM micrograph, -b-EDS spectrum of a particle in the heat treated sample showing Ti, Nb, Mn, Si, Al, Mg and Oxygen as its constituents.**

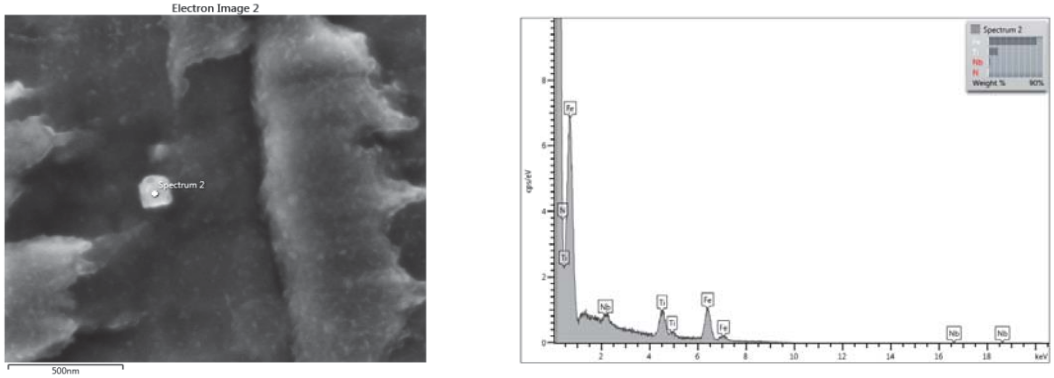

-a- -b-

Figure 5: EH46 sample heated to 1250 º C for 1min, followed by hot oil quenching (30K/sec)**, a-SEM micrograph, -b-EDS spectrum of a particle in the heat treated sample showing Ti, Nb and N as its constituents.**

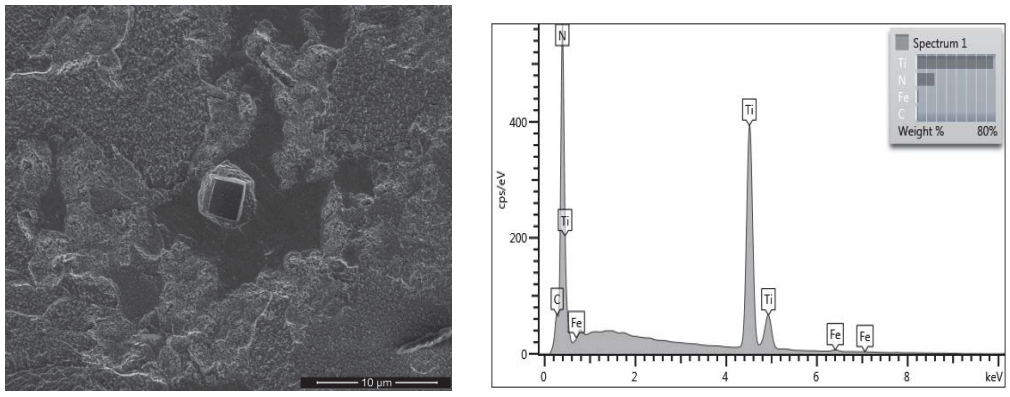

-a- -b-

Figure 6: EH46 sample heated to 1400ºC for 1min, followed by oil quenching (90K/sec)**, a-SEM micrograph, -b-EDS spectrum from a precipitate (of few microns) in the heat treated sample showing Ti and N as its constituents.**

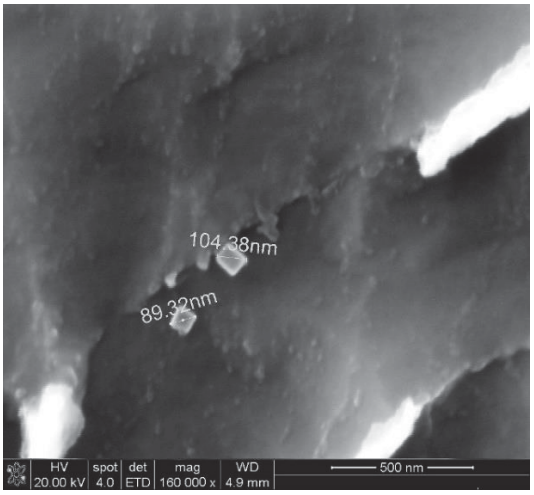

Figure 7: SEM micrograph of EH46 sample heated treated at 1240 ºC, held for 1min followed by oil quenching (90K/sec)**. Photographs taken from different parts of the same sample show size of TiN particles varies between 0.09 and 0.3 µm (90 and 300 nm).**

3.3 The Effect of the cooling rate on the size of TiN precipitates

To understand the effect of cooling rate on the size of TiN precipitates, unwelded samples of EH46 were heat treated at 1250°C and 1400°C and then were cooled at different cooling rates: oil quenching, hot oil quenching, air cooling and cooling inside furnace. Figures 8 and 9 show the relationship between the cooling rate and TiN particle size for samples heat treated at 1250°C and 1400 °C with holding times of 10 sec and 30 secs, respectively. Comparing Figures 8 and 9 reveals 30 secs holding time results in larger size particles; however, the Figures show among the effect of temperature, holding time and cooling rate, cooling rate plays a more prominent role in the size of precipitates in the heat treated EH46 samples.

Additionally, Figure 10 presents the size distribution of TiN particles (µm) in the heat treated samples cooled with hot oil quenching. It compares TiN particles size and distribution for different regimes of heat treatment conducted at two different temperatures of 1250 and 1400°C both held for two different holding times of 10 and 30 seconds. This Figure evidently shows heat treatment of up to 1400°C has led to larger precipitates ranging from 0.6 to 1.60 µm compared with precipitates of 0.5 to 0.5 µm in heat treated samples at 1250°C.

It is worth noting that, in a micro-alloyed steel, similar to this work, it has been shown that 10 seconds exposure to a high temperature has made a noticeable difference to the size and frequency of particles precipitating from the solid solution [16]. Hence, the importance of holding times as small as 10 seconds at temperatures above 1000°C on the precipitates should not be ignored.

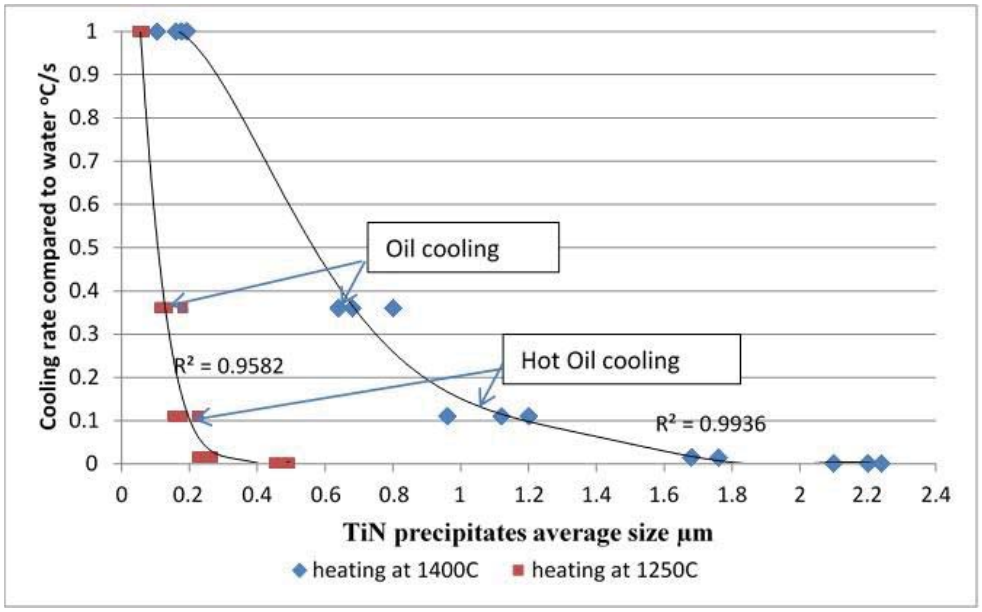

Figure 8: The correlation between TiN precipitates size (in µm) and the cooling rate (K/s) (holding time was kept constant at 10 sec). It shows the size of precipitates increased with decreasing the cooling rate.

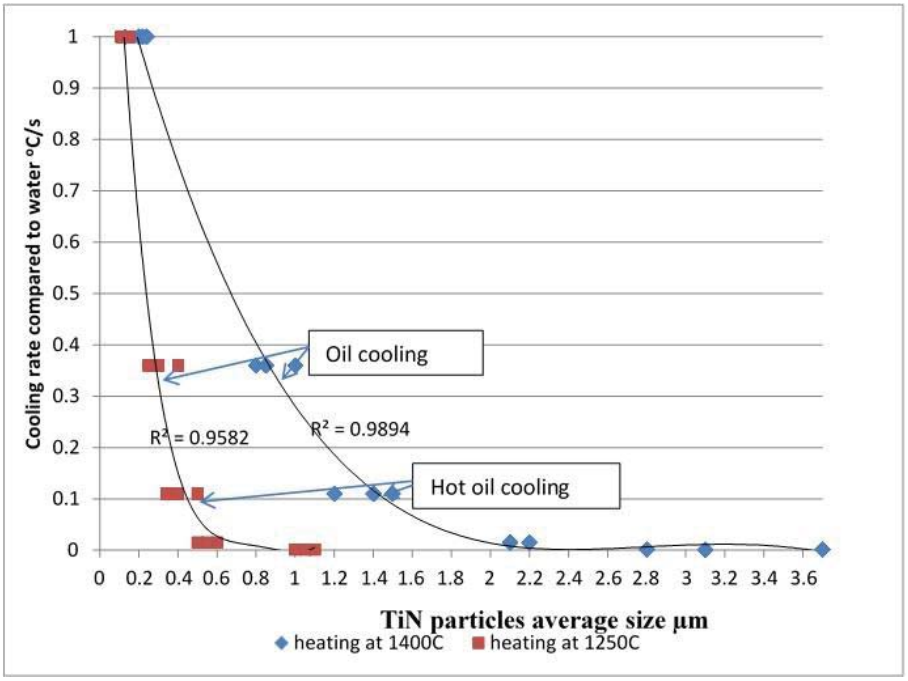

Figure 9: The correlation between size of TiN precipitates (in µm) and the cooling rate in K/s (holding time was 30 sec), the size of precipitates increased with decreasing the cooling rate.

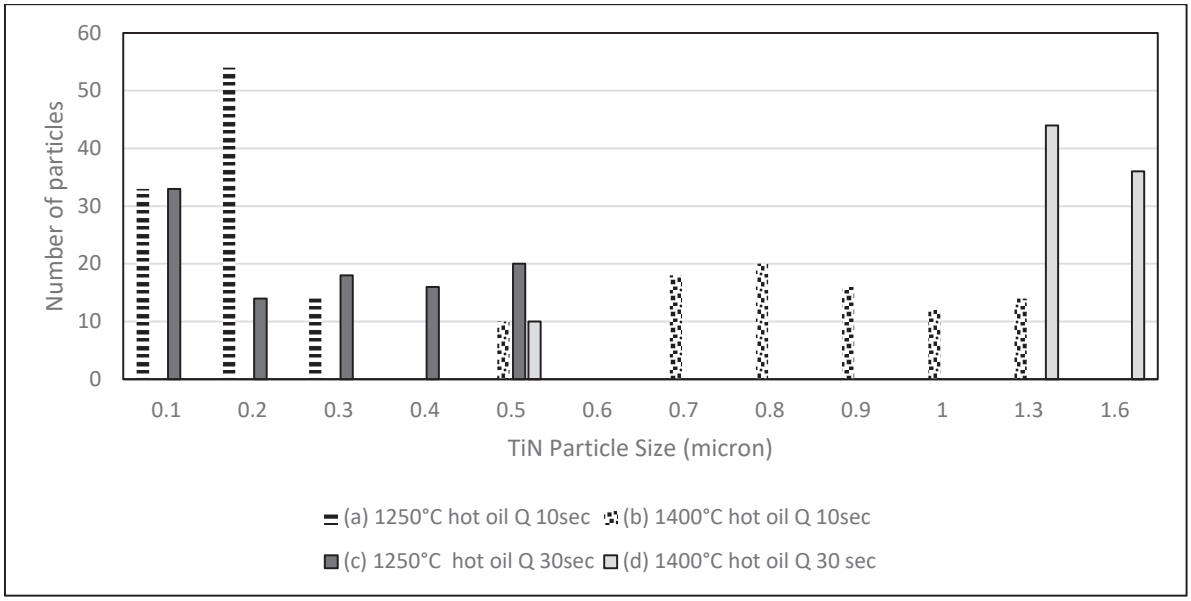

Figure 10: Histogram showing the size distribution of TiN particles observed in the samples heated at different temperatures (and times) followed by hot oil quenching -a- 1250°C for 10 sec, -b-1400°C for 10 sec, -c-1250°C for 30 sec and -d-1400°C for 30 sec.

3.4 TiN precipitates in FS welded Samples of EH46

SEM-EDS were also carried out to reveal the TiN particles precipitated in FS welded joints of EH46 steel. Given that FSW is a thermal process their particles size range was compared with the heat treated (unwelded) samples. To compare the effect of welding traverse speed on the constituents, Figure 11 -a- and -b- show high magnification micrographs of FSW EH46 W8 (150RPM, 50mm/min), whereas Figure 11 -c- and -d- show high magnification micrographs of FSW EH46 W9 (150RPM, 100mm/min). They clearly illustrate that the higher welding speed, traverse speed, (W9) resulted in finer precipitates with an average particle size of 0.5 μm compared with 0.6 μm for W8. To study the plunge/dwell period where there is no translational movement for FSW of EH46, Figure 12 shows high quantity of large TiN particles at the plunge period for sample W9.

To understand the role of process parameters on TiN particle sizes, this work also looked at the effect of tool rotational speed during plunge/dwell period which corresponds to the beginning of the FSW where there are no translational movements. Figure 13 -a- and -b- show TiN precipitates in EH46 W2 and W3 (plunge/dwell period) for region 1 (under tool shoulder). They show W3 with lower rotational speed and slightly shorter dwell time, contains smaller precipitates than W2 (0.5 μm compared with 0.7 μm).

Table 4 summarizes the TiN average particle size of EH46 W1 to W7 (plunge/dwell) at the shoulder-probe region. The table presents higher values for average particle size in W1 and W2, 0.6 and 0.7 μm respectively, compared with 0.5 μm for the remaining samples. This means higher rotational speed results in larger TiN precipitates on average, due to higher heat input.

To relate the role of FSW welding process parameters on particle frequency, in a histogram format Figures 14a and 164 illustrate the frequency distribution (%) of the TiN particle with varied size of 0.01 to 0.9 μm observed in W8 and W9 (steady state welding) and W1 to W7 (Plunge/Dwell), respectively. From comparing W8 and W9 in Figure 14a, clearly it can be seen that W9 (with higher transverse speed) produces finer particles. Figure 14b reveals that samples W3 to W7 present very similar particle distribution pattern. Given that they have very similar process parameters, this shows the reproducibility of the data.

As an example, Figure 15 shows one TiN particle with a size of 0.35 µm under probe side of W2 (region 2). This is very small compared to precipitates observed in region 1 of the weld (Figure 13a: 0.7 µm). This confirms region 1 experiences higher peak temperature.

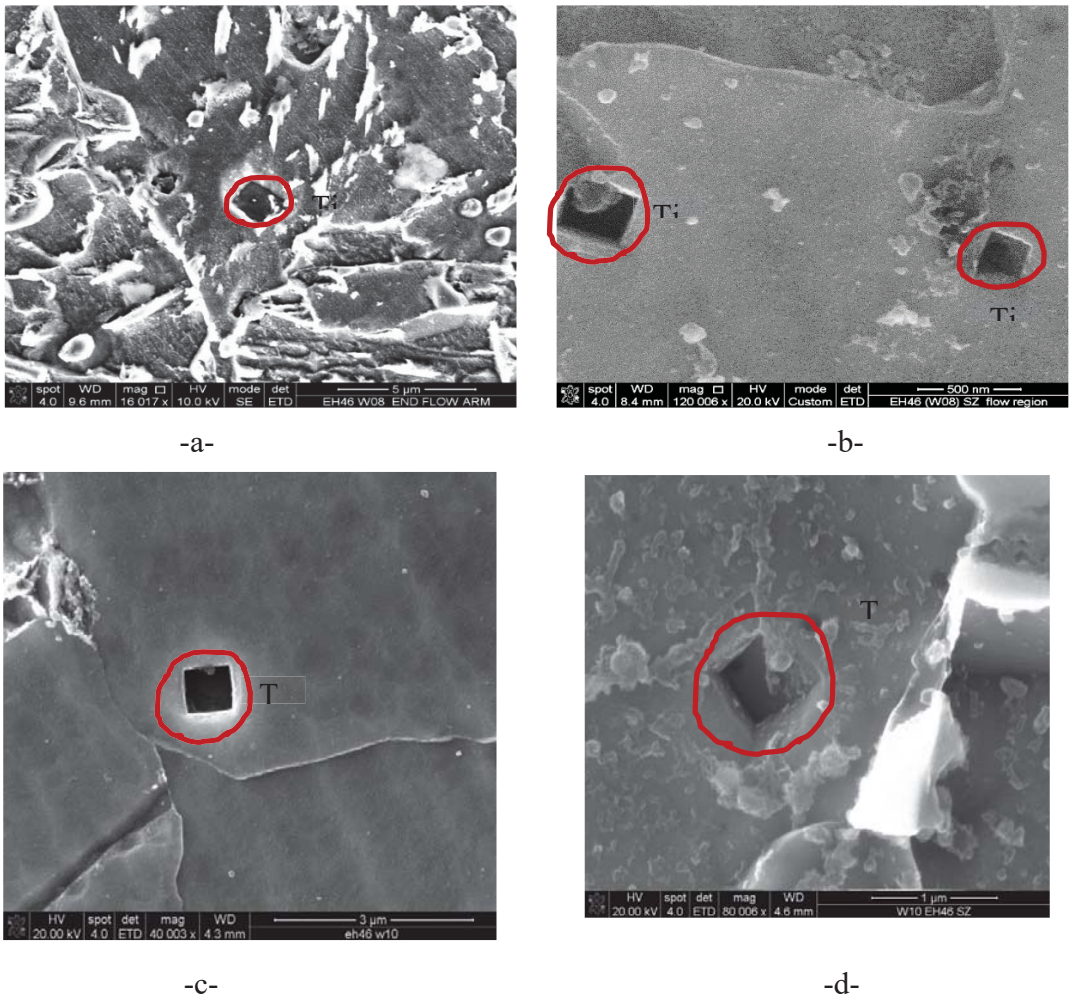

Figure 11: SEM micrographs of FSW EH46 samples -a- and -b- TiN particles in W8 (150RPM, 50mm/min), average size is 0.6µm, -c- and -d- TiN particles in W9 (150RPM, 100mm/min), average size is 0.5 µm.

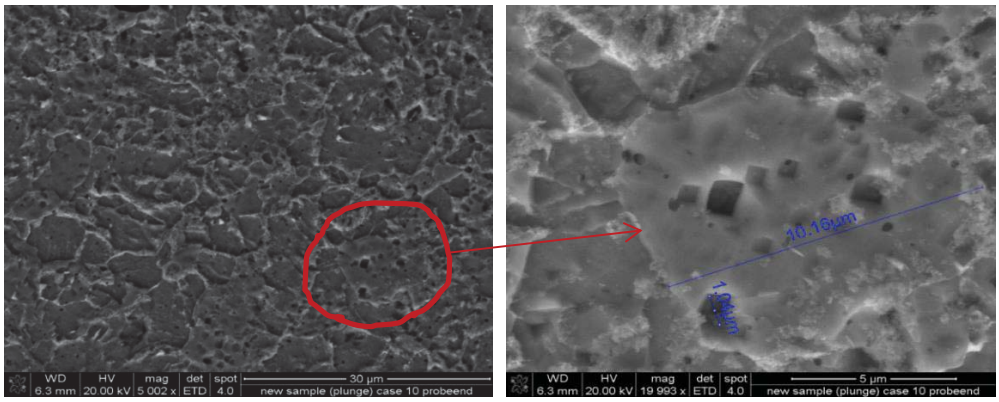

-a- -b-

Figure 12: SEM micrographs of EH46 W9 (during plunge/dwell period) probe-end, -a- low and -b- high Magnifications, showing numerous TiN precipitates (size varies between 0.7 to 1.5µm).

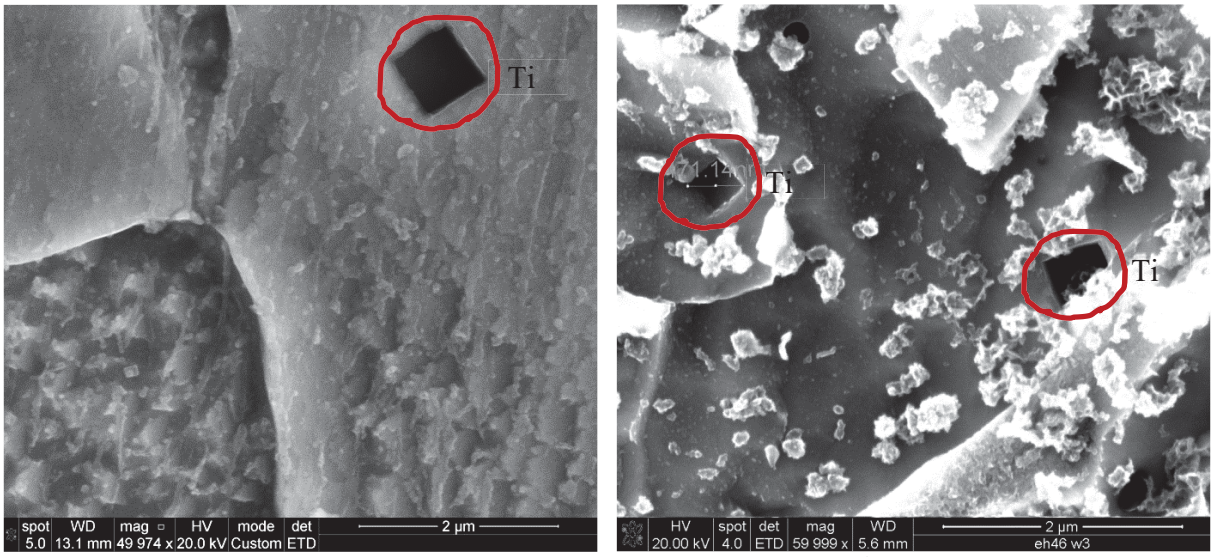

-a- -b-

Figure 13: SEM micrographs of EH46 (plunge/dwell period) region 1 under tool shoulder -a-W2 with an average TiN particle size of 0.7µm, -b- W3, with an average TiN particle size of 0.5µm.

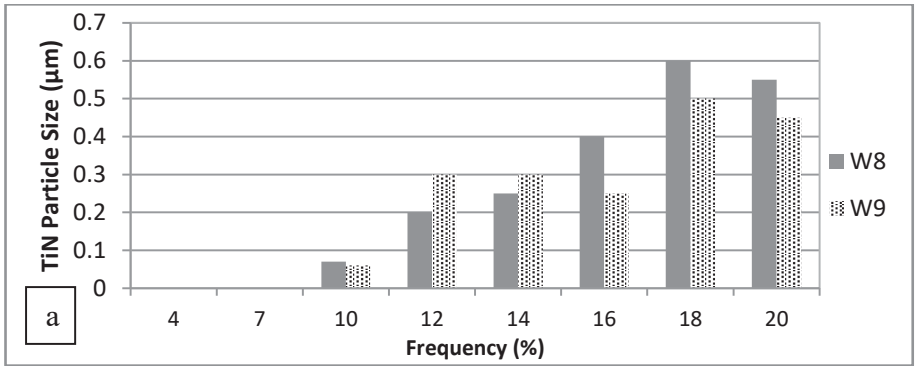

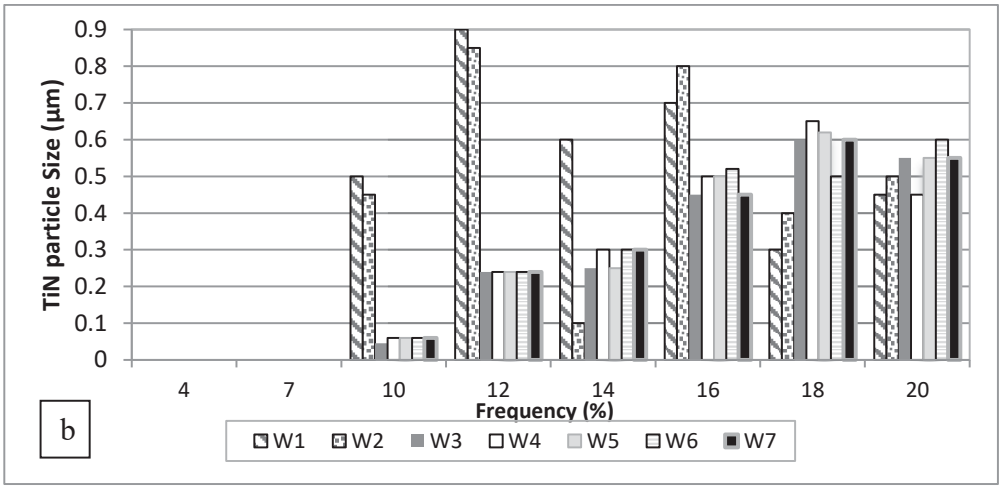

Figure 14: The Frequency Distribution (%) of the TiN particle size (µm) observed in -a- FSW EH46 W8 and W9 (steady state), -b- FSW EH46 W1 to W7 (Plunge/Dwell).

Table 4: TiN average particle size of samples W1 to W7 observed at the shoulder-probe region (Region 1): (Standard deviation value= 0.05 µm)

Weld No.	W1	W2	W3	W4	W5	W6	W7
TiN average particle size (µm)	0.6	0.7	0.5	0.5	0.5	0.5	0.5

Table 5: Interaction coefficients in molten steel at 1600ºC (1873K) [21].

Element	C	Si	Mn	P	Al	Ti	N
e_{Ti}^{J}	-0.165	0.050	0.0043	-0.64	12	0.013	-0.018
e_{N}^{J}	0.130	0.047	-0.02	0.045	-0.028	-0.53	…

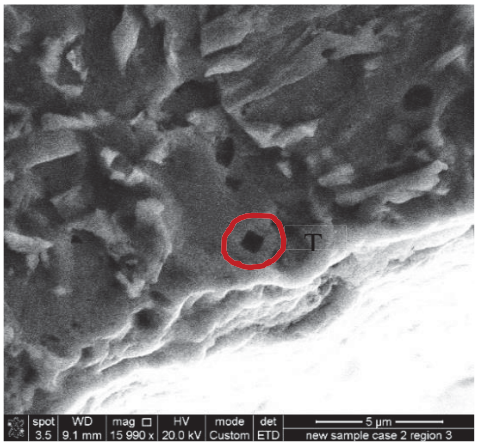

Figure 15: SEM Micrograph of sample W2 (plunge/dwell period) under the probe region showing TiN particles with average of 0.35 µm in size.

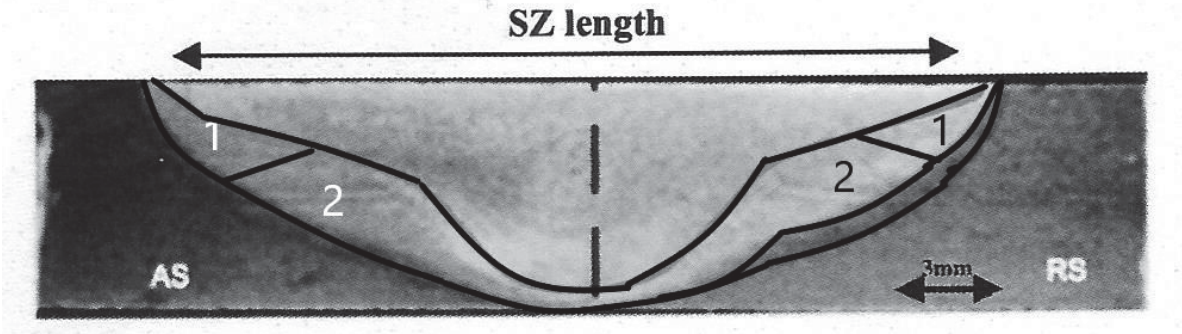

Figure 16. Two affected regions identified following the weld tool plunge trials sample W2, under the shoulder region (region 1) and around the probe side (region 2), both these regions are thermomechanically affected zones. Temperature predicted for region 1 to be reaching near 1400°C and for region 2 not to be greater than 1250°C.

4. Discussion:

4.1 Prior Austenite Grain Size (PAGS) and the effect of temperature

Figure 2 plots the correlation between PAGS and temperature for the heat treated samples heated in a temperature range of 1000 to 1400°C at holding time of 30sec then cooled by oil quenching. As the Figure shows PAGS increases gradually with a rise in peak temperature of heat treatment; however, it increases at a higher rate when the heating peak temperature exceeds 1300-1400°C. This is attributed to the role of Ti precipitates when exposed to high temperature heat treatment. Ti is proven to be a very effective element in controlling the austenite grain size and keeping it under 200µm when heated up to 1300°C. This is due to imposing of the pining forces at the grain boundaries [17]. In a previous study in a low carbon HSLA steel, (0.165 C, 1.11 Mn, and 0.34 wt% Ni), using a simple carbides and nitrides model Fernandez et al [18] theoretically determined the solubility temperature of TiN to be around 1682ºC. They studied the role of heat treatment on grain growth; given that their product was hot rolled, the grain growth began at lower temperatures and it was found that at short heat treatments (between 5 to 30 min) when the temperature exceeded 1200°C a drastic grain growth was observed; however, for longer heat treatment this critical temperature was lowered down to 1150°C. This was attributed to the dissolution of all carbides and nitrides precipitates during

heat treatment [18]. Similar to Fernandez et al [18], here PAGS, as shown in Figure 2, was increased significantly after reaching temperature of 1300-1400 °C which can indicate that most of particles responsible for grain refining by the effect of force pinning have been dissolved. It is worth noting that a study by Karmakar et al. [19] on the effects of microalloyed elements on PAGS has shown that Ti-Nb elements are the most effective elements in pinning the austenite grains when heat treated. Similar to this work, they reported that grain growth of austenite can occur when the temperature exceeds 1150 °C as a result of Ti-Nb dissolution. However, the abnormal grain growth in austenite was reported to occur slightly at higher temperature than here, after reaching a temperature of 1400 °C due to complete dissolution of TiN particles.
It is worth noting that here only the role of temperature on pinning effect of TiN precipitates is taken into account and not the role of deformation and the introduction of stress and therefore, strain. Deformation leads to recovery and/or recrystallization which results in softening. However, small precipitates can delay the recovery and recrystallization and therefore, grain growth can be prohibited or delayed if strain is low; however, at higher strains they become less effective due to increased rate of recovery and recrystallization. This means increasing the amount of deformation leaves a very limited time for nucleation of precipitates. Some measurements of such behavior can be found elsewhere [20].

4.2. Thermodynamics of TiN formation in low alloy steel

Precipitation behavior of TiN in low alloy steels during solidification and hot rolling (hot deformation) are carefully studied, this is done through application of current chemical content to thermodynamics formulae relevant to this grade.

$$[\boldsymbol{Ti}] + [\boldsymbol{N}] = \boldsymbol{TiN}\ (\boldsymbol{s})\ ,\ \Delta G = \Delta G^{\theta} + RT \ln \frac{1}{f_{Ti}.[Ti].f_N.[N]} \quad (2)$$

$$\Delta G^{\theta} = -291000 + 107.91\,T \quad (3)$$

where f_{Ti} and F_N are the activity coefficient of Ti and N in molten steel, respectively [21]. The activity coefficients of Ti and N can be obtained using the following equations, chemical content of the steel and the interaction coefficient values of each element in the molten steel listed at Table 5.

$$lgf_{Ti} = \left(\frac{2557}{T} - 0.365\right) \sum \left(e^{j}_{Ti\ (1873K)}[\%j]\right) \quad (4)$$

$$lgf_{N} = \left(\frac{3280}{T} - 0.75\right) \sum \left(e^{j}_{N\ (1873K)}[\%j]\right) \quad (5)$$

Using equations 2 to 5 and data in Tables 1 and 5 results in Gibbs free energy equation for dissolution of TiN in the studied alloy as follows:

$$\Delta G = -291000 + 181.996T \quad (6)$$

When the reaction reaches equilibrium that ΔG=0 and therefore T= 1325.94ºC. Therefore, based on these calculations for TiN to precipitate at this alloy temperature must reach about 1326ºC. This calculation does not take into account the role of hot deformation in inducing precipitates, but as discussed in the above section this won't be significant.

4.3 TiN precipitates in the heat treated samples

Samples which were heat treated at 1000 °C did not show evidence of TiN precipitates under the SEM investigation. This can be due to the fact that the TiN precipitation usually occurs at temperatures exceeding 1000 °C [12]. Other samples which experienced higher temperatures showed different size of Ti precipitates including TiN shown in SEM images and EDS spectrum in Figures 4 to 6. In this work, heating up to 1130°C with different cooling rates resulted in precipitation of Ti with other elements including Al, Nb, S, O, V, P as shown in Figure 4. The current work is only focused on TiN precipitates and thus the other Ti precipitates

will not be discussed. Samples heated at 1240°C (Figure 5) had TiN precipitation with average size of 0.1μm (100nm) accompanied with Nb whereas, heating up to 1400°C resulted in a coarser precipitation of TiN (0.5-1μm) as shown in Figure 6. Cooling of samples presented in Figures 4 to 6 was achieved by quenching in hot oil of temperature of 100°C; this produced a cooling rate of 30°C/sec which is the expected cooling rate that produces a ferrite/ cementite aggregate microstructure [22] similar to the FSW samples microstructure observed in this work. This suggests the cooling rate of FSW samples would have been close to this rate. Ti usually has a strong affinity to form nitrides, oxides and even sulphides before forming carbides [23], adding elements forming nitrides (e.g. V, Ti) to steel leads to the precipitation of pure V (or Ti) nitrides and thermal stability of nitrides is higher compared to equivalent carbides [24]. It is known that pure TiN requires low amount of Ti in the steel matrix (less than 0.025wt%) and also low carbon content, otherwise other precipitates such as (Mn, Ti)S or Ti (C,N) will be more dominant precipitate depending on the composition of steel [25-26].

4.4 The Effects of the cooling rate on TiN particle size

Figures 8 and 9 show the relationship between the cooling rate and the average size of TiN particles for two different heat treatment temperatures and two different holding times. The TiN particle size increases significantly when cooling rate decreases, especially when samples cooled inside a furnace. It is evident that TiN can precipitate even under a fast cooling regime such as oil quenching. A work carried out on low carbon steel (0.12-0.14%C) with a Ti% 0.006-0.013 [8] showed that cubic TiN can be precipitated after heating up to 1526°C where there were no pre-existing TiN precipitates and then cooling down to 1000°C at various cooling rates. However, compared to this work, in their case precipitates were very small and were formed as clusters of particles [8]. This suggests that the temperature, i.e. heat treatment temperature is a key factor in forming the precipitates rather than the cooling rate. The cooling rate only influenced the size and frequency of the precipitates but not their occurrence and formation.

The slower cooling rate means that the TiN precipitates can nucleate in longer period at temperature and thus leads to coarsening of the precipitates. This has been observed previously [9] where it is shown that in addition to heating and cooling conditions, interactions between steel composition and processing were also significant factors in TiN precipitates size and distribution. It is concluded that final particle size is influenced by a competition between coarsening and completion of precipitation.

Increasing the holding time to 30 sec at 1400°C with a very slow cooling rate (cooling inside a furnace) has resulted in coarsening of TiN particles exhibiting particles exceeding 3μm in size, as shown in Figures 9 and 10 d. The faster cooling rate can lead to a larger undercooling and higher supersaturating of solute for precipitation and thus larger driving force, so more fine particles will form at lower temperature. Figure 10 shows the size frequency (%) of TiN particles when heating to 1250 and 1400 °C both for 10 and 30 secs. The Figure shows TiN particle size increased with an increase in the temperature, the frequency of large particle size also increased when soaking time increased. This was due to formation of more TiN precipitates. With holding longer at the temperature, precipitate nucleation may occur over a prolonged period and hence it is possible for small particles nucleated later to co-exist with larger particles that formed earlier. This leads to particle size variation as shown in Figure 10.

4.5 TiN precipitates in FSW samples of EH46

SEM micrographs of EH46 FSW samples (W8 and W9) exhibit precipitations of TiN in the top of the stir zone (SZ) with average size of 0.6 μm (600nm) and 0.5 μm (500nm) in the steady state period as shown in Figures 11 a to d, respectively. The TiN particle size exceeded 1μm in the plunge period (the start of welding where the tool is rotating but not moving) as shown

in Figures 12 a and b. In these Figures, eight TiN particles (size is 0.7μm to 1.5μm) can be counted inside a 10 μm ferrite grain. This coarsening of TiN particles is believed to be resulted from exposure to high temperature and slow cooling rate.
The plunge/dwell cases of EH46 W1 to W7 have also been investigated for TiN precipitates, Figures 13 a and b show TiN precipitates of W2 and W3 respectively at region 1 under tool shoulder. An average size of 0.70 and 0.5 μm is calculated for particles in region 1 of W2 and W3, respectively. The average size of TiN particles is calculated and listed at Table 4 (with an accuracy of ±0.05 μm). Figure 15 shows TiN particle at region 2 under tool probe with average size of 0.35μm. This decrease in TiN particle size from 0.70 μm to 0.35 μm can be attributed to a lower peak temperature under probe (region 2) compared to the region under shoulder (region 1).

4.6 Comparison of FSW and heat treatments in terms of TiN Precipitation

As shown in Figure 10 it is evident that heat treatments at 1250°C followed by hot oil quenching resulted in TiN precipitates with size of 0.2 to 0.5 μm similar to W9 sample, which contains TiN precipitates of almost the same size and frequency (Figure 14a). W8 shows coarser TiN particles with average of 0.6 μm which suggests slower cooling rate than in W9 as the tool traverse speed was halved the speed of W9. Cooling rate is estimated to be in the range of 10 to 30 K/s based on the comparison with results of heat treatments with a minimum peak temperature of 1250 °C. The ferrite grain shown in Figure 12 with average grain size of 10 μm contains eight large cubic precipitates of TiN which are ranging from 0.7 to 1.5 μm. The large size of these precepitates indicates that the material has been exposed to a very high temperature (may have reached 1400 °C, the cooling rate was slow enough to form these precipitates, expected less than 10K/s). It is, however, unlikly these large precipetates can play any significant role in pinning the austenite graine during heating. The reduction in pinning forces due to temperature increase higher than 1200 °C was reported by Karmaker et al. [19] and also by Gong et al. [16] where the austenite grains experienced coarsenning resulted from Ti-Nb dissolution. Therefore, similarly, the coarse ferrite grain at the probe end of W9 during the plunge period shown in Figure 12 which exceeds 10μm can be attributed to the loss of the pinning force of precipitates, in addition to the high temperature and slow cooling rate. As discussed in section 4.1 grain growth could also be attributed to the role of deformation through increased rate of recovery and recrystallisation and not only the removal of pinning effect.
In the plunge cases of W1 to W7 SEM examinations have shown occurance of TiN precipitation in the shoulder-probe region (as shown in Figure 13). The average size of these precipitates are summarised and presented in Table 4. The table shows W1 and W2 exhibit larger average size of TiN particles (0.6-0.7 μm) than other samples, W3 to W7 (0.5μm). This has been attributed to having higher tool rotational speed (200RPM) for W1 and W2 compared to other welds which have a lower tool rotational speed (120RPM). The higher tool speed could have caused higher peak temperature and thus slower cooling rate expected. This in turn can lead to TiN particle coarsening as discusesed previously. The temperature of W1 and W2 at the shoulder-probe is expected to exceed 1250°C but not to reach 1400 °C according to the heat treatments results shown in Figures 8 and 9. W3 to W7 peaks temperatures are expected to reach 1250 °C with a cooling rate range of 20 to 30K/s.
Figure 15 shows TiN particle at the probe side of W2, the average calculated size of TiN particles was 0.35μm which is smaller than that found at the shoulder-probe region. The reduction in TiN particles size can be attributed to a lower peak temperatures and faster cooling rate. This result agrees with previous works [27-29] that shows that heat generation in FSW is spatial and the maximum temperature is always at the tool/workpiece contact region.
Figure 16 illustrates the temperature distribution under the tool based on temperature predictions made here for one of the samples (W2).

As shown understanding TiN formation during heat treatments can be a very useful method in estimating peak temperature and cooling rate of the FSW joints of EH46 steel and thus can assist with determining suitable rotational and traverse speeds of the tool to produce sound joints without a need for using thermocouples or thermal imaging camera. But it is worth noting that FSW is not purely a thermal process and as a result some of precipitates may have been strain induced. However, this has not been evidently proven. It is known that diffusivity of Ti must be sufficient for the TiN precipitates to grow or coarsen. Additionally, the presence of dislocations and grain boundaries which have an impact on the diffusion can play an important role. It is previously shown that an increase in atom mobility due to the defect presence results in faster Ostwald ripening of the existing particles [30]. It is also shown [9] that deformation increased dislocation densities and hence assisted diffusion mechanism. Deformation could also move jog-dragging screw dislocations, and hence a line of vacancies in the matrix can be formed. This itself can enhance bulk diffusion and assist with Ostwald ripening. Based on the above, "deformation enhanced coarsening" can be a possible mechanism for some drastic increase in particle size experienced after rolling in steel [31]. However, there has not been any work demonstrating the role of deformation/ strain leading to a significant change in formation temperature of TiN precipitates in steel. This suggests the present work which has only taken thermal process into effect is not very unrealistic and hence can provide a rather good estimation for peak temperature and cooling rate in FSW of EH46 steel.

Conclusions

The work presented is the first attempt to estimate the temperature in the stirred zone and cooling rate of FSW of steel joints from precipitates formed after welding. After undertaking a series of heat treatments to produce varied temperature and cooling rate conditions, the work compared the heat treated samples with samples welded using Friction Stir Welding technique with few different welding variables in EH46 steel samples. It looked at the role of rotational speed and traverse speed on the peak temperature at the tool/joint interface. From the results the following conclusions can be drawn:

1. Prior Austenite grains coarsened dramatically when heating temperature of unwelded samples exceeded 1300-1400°C. This was attributed to the reduction in pining forces resulted from the dissolution of Ti/ Ti-Nb based particles and formation of new coarse cubic precipitates of TiN. Thermodynamic calculations estimated the dissolution temperature of TiN to be ~1326°C.
2. It is found that the temperature at the weld/tool interface is the main driver for TiN formation, and TiN begins to precipitate when the sample temperature exceeds 1100°C. Pure TiN can precipitate at high temperatures in the range of 1250 -1400°C. However, their size was also influenced by the cooling rate and the soaking time. This was more profound at higher heat treatment temperatures.
3. The average size of TiN particles increased with decreasing cooling rate, a maximum precipitate size which exceeded 3μm was found when unwelded EH46 samples heated to 1400°C and then cooled slowly inside a furnace with a cooling rate of 0.35 K/s.
4. When EH46 heated to two different temperatures of 1250 and 1400°C followed by cooling at different cooling rates quenching in oil (90K/sec), quenching in hot oil with a temperature of 150°C (30K/sec), still air cooling and cooling inside a furnace (0.35K/sec) and held at two different holding times of 10 and 30 secs, it is found that the cooling rate, and not the temperature, played a prominent role in forming smaller precipitates at higher cooling rates (0.2-0.4 μm for cooling with a rate of 240K/sec). However, in lower cooling rates such as cooling in furnace heat treatment had more profound effect; i.e. lower heat treatment temperature led to smaller size precipitates.

5. Using this new technique for samples FS welded (plunge and dwell stage) under two different rotational speeds of 120 and 200 RPM revealed the temperature in their stirred zone is to be approximately 1250 and 1400°C, respectively. For samples welded under rotational and traverse speeds of 150 RPM and 50 mm/min the temperature in the stirred zone is to be approximately 1400°C.
Overall, it is shown to estimate the peak temperature of weld/joint interface and associated cooling rate for Friction Stir Welding from TiN precipitates and their size distribution provides a valid basis for an inexpensive method to replace other technique such as utilization of thermocouples or thermal imaging cameras.

Acknowledgement
The authors would like to thank The Welding Institute (TWI) Yorkshire for providing FSW samples of steel and related operational data, also special thanks to Mr Stuart Creasy at Sheffield Hallam University for helping in obtaining clear SEM images at high magnification.

References
1. W.M. Thomas, E.D. Nicholas, J.C. Needham, M.G. Murch, P. Templesmith and C.J. Dawes: Friction Stir Butt Welding, International Patent No. PCT/GB92/02203 (1991).
2. S.A. Hussein, S. Thiru, R. Izamshah and A.S.M.D. Tahir: *Advances in Mat. Sci. & Eng.*, 2014, 8 pages.
3. P. Carlone and G.S. Palazzo: *Metallogr. Microstruct. Anal.*, 2013, vol. 2, pp. 213-222.
4. J. Mezyk and S. Kowieski: *Solid State Phenomena*, 2015, vol. 220-221, pp. 859-863.
5. Z.H. Zhang, W.Y. Li, J.L. Li and Y.J. Chao: *Int. J. Adv. Manuf. Technol.*, 2014, vol. 73, pp. 1213-1218.
6. A. Arora, T. DebRoy and K.H.D.H. Bhadeshia: *Acta Mater.*, 2011, vol. 59, pp. 2020-2028.
7. L. Wang, C.M. Davies, R.C. Wimpory, L.Y. Xie and K.M. Nikbin: *Materials at High Temperature*, 2010, vol. 27, pp. 167-178.
8. J. Stock, C.M. Enloe, R.J. O´Malley, and K.O. Findley: *AIST Transactions*, 2014, vol. 11, pp. 180-186.
9. M.T. Nagata, J.G. Speer and D.K. Matlock: *Metall. Mater. Trans. A*, 2002, vol. 33A, pp. 3099-3110.
10. K.A. EL-Fawakhry, M.F. Mekkawy, M.L. Mishreky, and M.M. Eissa: *ISIJ International*, 1991, vol. 31, pp. 1020-1025.
11. M.L. Wang, G.G. Cheng, S.T. Qiu, P. Zhao, and Y. Gan: *International Journal of Minerals, Metallurgy and Materials*, 2010, vol.17, pp. 276-281.
12. S.G. Hong, H.J Jun, K.B. Kang and C.G. Park: *Scr. Mater.*, 2003, vol. 48, pp. 1201–1206.
13. D.M. Failla, 2009, Friction Stir Welding and Microstructure Simulation of HSLA-65 and Austenitic Stainless Steels, MSc Thesis, The Ohio State University.
14. S.F. Medina, A. Quispe and M. Gomez: *Metall. Mater. Trans. A.*, 2014, vol. 45A, pp. 1524–1539.
15. Z.H. Zhu and S.T. Qiu: *Advanced Materials Research*, vols. 535-537, pp. 633-638.
16. P. Gong, E.J. Palmiere and W.M. Rainforth: *Acta Mater.*, 2015, vol. 97, pp. 392-403.
17. L.J. Cuddy: "The Effect of Microalloy Concentration on the Recrystallization of Austenite During Hot Deformation", In: A. J. DeArdo, G. A. Ratz, and P. J. Wray, eds. Thermomechanical processing of microalloyed austenite. Pittsburgh, USA: TMS-AIME, 1981: 129-140.
18. J. Fernández, S. Illescas and J.M. Guilemany: *Mater. Letters*, 2007, vol. 61, pp. 2389–2392.
19. A. Karmakar, S. Kundu, S. Roy, S. Neogy, D. Srivastava and D. Chakrabarti: *Mater. Sci. Tech.*, 2014, vol. 30, pp. 653-664.
20. J. Kunze, C. Mickel, G. Backmann, B. Beyer, M. Reibold, C. Klinkenberg, *Steel Research*, 1997, vol. 68 (10), pp. 441-449.
21. T-P Qu, J. Tian, K-I Chen, Z Xu, D-Y Wang: Ironmaking & Steelmaking, 2019, vol. 46 (4), pp. 353-358.

22. S.F. Di Martino and G. Thewlis: *Metall. Mater. Trans.* A., 2014, vol. 45A, pp. 579-594.
23. A.J. DeArdo: *International Materials Reviews*, 2003, vol. 48, pp. 371–402.
24. G. Stein, W. Kirschner and J. Lueng, Application of Nitrogen-Alloyed Martensitic Stainless Steels in the Aviation Industry, 1997, Eds: E.G. Nisbett and A.S. Melilli , Steel Forgings: Second volume, ASTM Special Technical Publication, pp104-115.
25. T. Shiraiwa and N. Fujino, "Electron Probe Microanalysis of Ti(C, N) and Zr(C, N) in Steel", 1969, In: Möllenstedt G., Gaukler K.H. (eds) Vth International Congress on X-Ray Optics and Microanalysis, Springer, Berlin, Heidelberg, pp 531-534.
26. M. Hua, C.I. Garcia, and A.J. DeArdo: Metall. Mat. Trans. A, 1997, vol. 28A, pp. 1769-80.
27. H. Schmidt and J. Hattel: *Modelling and Simulation in Materials Science and Engineering*, 2005, vol. 13, pp.77–93.
28. H.B. Schmidt and J.H. Hattel: *Scri. Mater.*, 2008, vol. 58, pp.332–337.
29. P.A. Colegrove, H.R. Shercliff and R. Zettler: *Science and Technology of Welding and Joining*, 2007, vol. 12, pp. 284-297.
30. R.K. Gibbs, R.C. Peterson and B.A. Parker: Proc. Int. Conf. on Processing, Microstructure and Properties of Microalloyed and Other Modern High Strength Low Alloy Steels, Iron and Steel Society, Warrendale, PA, 1992, pp. 201-207.
31. S. Matsuda and K. Okumura: *Trans. Iron Steel Inst. Jpn.*, 1978, vol. 18, p. 198.

List of Figures:

Figure 1: Representation of the positioning of the seven plunge trials for EH46 steel plates.

Figure 2: Variation of prior austenite grain size with temperature for heat treated samples of EH46 in temperature range of 1000-1500°C with holding time of 30sec.

Figure 3: SEM micrograph showing Ti and Ti-Nb based particles in the as-received EH46.

Figure 4: EH46 sample, heated to 1130°C for 1min, followed by hot oil quenching (30K/sec), a-SEM micrograph, -b-EDS spectrum of a particle in the heat treated sample showing Ti, Nb, Mn, Si, Al, Mg and Oxygen as its constituents.

Figure 5: EH46 sample heated to 1250°C for 1min, followed by hot oil quenching (30K/sec), a-SEM image, -b-EDS spectrum of a particle in the heat treated sample showing Ti, Nb and N as its constituents.

Figure 6: EH46 sample heated to 1400°C for 1min, followed by oil quenching (90K/sec), a-SEM image, -b-EDS spectrum from a precipitate (of few microns) in the heat treated sample showing Ti and N as its constituents.

Figure 7: SEM micrograph of EH46 sample heated treated at 1240°C, held for 1min followed by oil quenching (90K/sec). Photographs taken from different parts of the same sample shows size of TiN particles varies between 0.09 and 0.3 μm (90 and 300 nm).

Figure 8: The correlation between size of TiN precipitates (in μm) and the cooling rate in K/s (holding time was 10 sec), the size of precipitates increased with decreasing the cooling rate.

Figure 9: The correlation between size of TiN precipitates (in μm) and the cooling rate in K/s (holding time was 30 sec), the size of precipitates increased with decreasing the cooling rate.

Figure 10: Histogram showing the size distribution of TiN particles observed in the samples heated at different temperatures (and times) followed by hot oil quenching -a-1250°C for 10 sec, -b-1400°C for 10 sec, -c-1250°C for 30 sec and -d-1400°C for 30 sec.

Figure 11: SEM micrographs of FSW EH46 samples -a- and -b- TiN particles in W8 (150RPM, 50mm/min), average size is 0.6µm, -c- and -d- TiN particles in W9 (150RPM, 100mm/min), average size is 0.5 µm.

Figure 12: SEM micrographs of EH46 W9 (during plunge/dwell period) probe-end, -a-low and -b- high Magnifications, showing numerous TiN precipitates (size varies between 0.7 to 1.5µm).

Figure 13: SEM micrographs of EH46 (plunge/dwell period) region 1 under tool shoulder -a- W2 with an average TiN particle size of 0.7µm, -b- W3, with an average TiN particle size of 0.5µm.

Figure 14: The Frequency Distribution (%) of the TiN particle size (µm) observed in -a- FSW EH46 W8 and W9 (steady state), -b- FSW EH46 W1 to W7 (Plunge/Dwell).

Figure 15: SEM Micrograph of sample W2 (plunge/dwell period) under the probe region showing TiN particles with average of 0.35 µm in size.

Figure 16. Two affected regions identified following the weld tool plunge trials sample W2, under the shoulder region (region 1) and around the probe side (region 2), both these regions are thermomechanically affected zones. Temperature predicted for region 1 to be reaching near 1400°C and for region 2 not to be greater than 1250°C.

Table 1: Chemical composition (wt%) **of EH46 Steel Grade as received (composition is provided by the manufacturer).**

C	Si	Mn	P	S	Al	N	Nb	V	Ti
0.20	0.55	1.7	0.03	0.03	0.015	0.02	0.03	0.10	0.02

Table 2: The welding parameters for FS welded EH46 plunge/dwell samples (W1-W7).

Weld Trial No.	Tool rotational speed ω (RPM) at dwell period	Max. Axial (Plunge) force (F_z) KN	Max. longitudinal force (F_x) KN	Max. Torque (M) N.m	Plunge Depth (Z) mm from FSW machine	Dwell Time (t) sec at dwell period
W1	200	157	17	498	13	6
W2	200	127	17	471	13	8
W3	120	116	21	598	13	7
W4	120	126	20	549	13	6
W5	120	115	17	532	13	7
W6	120	105	18	583	13	7
W7	120	119	20	548	13	7

Table 3: Welding parameters for FS welded EH46 steel at steady state condition (W8 and W9).

Tool rotational speed RPM	Traverse speed mm/min	Rotational/ Traverse speeds (rev/mm)	average spindle Torque N.m	average tool Torque N.m	Axial force (average) KN	longitudinal force (average) KN	Representation of Heat Input $(\frac{\omega \times torque}{V})$ (rev. KN)
150	50	3	300	114	66	13	342
150	100	1.5	450	171	72	14	256.5

Table 4: TiN average particle size of samples W1 to W7 observed at the shoulder-probe region (Region 1). (Standard deviation value= 0.05 µm)

Weld No.	W1	W2	W3	W4	W5	W6	W7
TiN average particle size (µm)	0.6	0.7	0.5	0.5	0.5	0.5	0.5

Table 5: Interaction coefficients in molten steel at 1600ºC (1873K) [21].

Element	C	Si	Mn	P	Al	Ti	N
e_{Ti}^{J}	-0.165	0.050	0.0043	-0.64	12	0.013	-0.018
e_{N}^{J}	0.130	0.047	-0.02	0.045	-0.028	-0.53	…